Observation of increased space-charge limited thermionic electron emission current by neutral gas ionization in a weakly-ionized deuterium plasma

E. M. Hollmann, J. H. Yu, R. P. Doerner, D. Nishijima, and R. P. Seraydarian
University of California, San Diego, 9500 Gilman Dr., La Jolla, California 92093-0417, USA

(Received 13 July 2015; accepted 25 August 2015; published online 9 September 2015)

The thermionic electron emission current emitted from a laser-produced hot spot on a tungsten target in weakly-ionized deuterium plasma is measured. It is found to be one to two orders of magnitude larger than expected for bipolar space charge limited thermionic emission current assuming an unperturbed background plasma. This difference is attributed to the plasma being modified by ionization of background neutrals by the emitted electrons. This result indicates that the allowable level of emitted thermionic electron current can be significantly enhanced in weakly-ionized plasmas due to the presence of large neutral densities. © *2015 AIP Publishing LLC*.
[http://dx.doi.org/10.1063/1.4930160]

I. INTRODUCTION

Electron emission from plasma-facing surfaces is thought to play a central role in the plasma-material interactions of magnetic fusion devices. In the absence of surface electron emission, the sheath voltage tends to shield the surface from electron heat flux. However, as surface electron emission increases, either from thermionic emission,[1] secondary electron emission, or field emission from fine material structures,[2] the sheath voltage decreases, allowing increased electron heat flux. The resulting increased material heating can lead to localized hot spot formation and arcing[3] which can in turn lead to increased material erosion and impurity release into the plasma.[4] Research in this area is therefore important for accurate prediction of plasma-facing surface erosion and core contamination in future tokamaks.

The increase in thermionic emission current as a material surface is heated and is described by the Richardson-Dushman equation

$$j_{Rich} = A_R T^2 \exp(-\Theta_w/T), \tag{1}$$

where T is the surface temperature, A_R the Richardson constant, and Θ_w the work function. For tungsten, we use the standard value of $A_R = 120\,\frac{\mathrm{A}}{\mathrm{cm^2 K^2}}$ (Ref. 5) and $\Theta_W = 4.5\,\mathrm{eV} = 5.2 \times 10^4 \mathrm{K}$. For sufficient emission current, buildup of space charge at the surface stops further increases in the net thermionic electron ("thermoelectron") current leaving the surface. The case of a floating target assuming ambipolar flow was derived previously.[6] In this case, the sheath potential drops from $\phi_{Sheath} \approx 3T_e$ to a limiting value of $\phi_{Sheath} \approx 0.7T_e$ as the thermoelectron current is increased. The resulting space-charge limited thermoelectron current is of order 10 times the plasma ion current to the target. The floating ambipolar approximation is not necessarily applicable to unipolar arcs in fusion devices, however, where the electron current emitted from a local hot spot can return through adjacent conducting surfaces.[1]

For the more general case of space-charge limited thermoelectron current at arbitrary sheath potential, a modified Child-Langmuir expression was proposed, using the Child-Langmuir current density

$$j_{CL} = \frac{4}{9}\varepsilon_0 \sqrt{\frac{2e}{m_e}} \frac{\phi_{Sheath}^{3/2}}{d^2}, \tag{2}$$

but using the sheath potential ϕ_{Sheath} (rather than the usual electrode potential difference) and $d \approx 2.2\lambda_D$, where λ_D is the Debye length (rather than the usual inter-electrode gap).[7] Subsequently, an improved bipolar flow expression at arbitrary sheath potential was derived assuming zero ion temperature but including finite thermoelectron temperature.[8,9] For zero thermoelectron temperature, the resulting current is

$$j_{IB} = j_{sat}/\alpha_{sc} = \frac{G\sqrt{\pi\Phi_w}}{1+G}\sqrt{\frac{2m_i}{\pi m_e}} j_{sat}, \tag{3}$$

where j_{sat} is the ion saturation current supplied by the plasma, $\Phi_w \equiv e\phi_{Sheath}/k_B T_e$ is the normalized sheath potential, and $G(\Phi_w)$ is a function of normalized sheath potential defined in Ref. 9.

The total current going into the target is given by[9]

$$j_{tot}/j_{sat} = \sqrt{\frac{1+G}{1+G/(-2\Phi_w)}} - \frac{1}{2(1+G)}\sqrt{\frac{2m_i}{\pi m_e}}\exp(-\Phi_w) + \frac{G\sqrt{\pi\Phi_w}}{1+G}\sqrt{\frac{2m_i}{\pi m_e}}. \tag{4}$$

In Eq. (4), the first term is due to incoming plasma ions, the second due to incoming plasma electrons, and the third due to the outgoing thermoelectrons. For the experiments presented here, with $\Phi_w \approx 2-25$, the last term is expected to dominate by a factor of 10–50, so measuring the total perturbed current entering the target during the laser pulse is expected to give a reasonable measure of the thermoelectron current.

Previous experiments were performed to test these predictions using a large biased tungsten plate inserted into a helium plasma.[10] The experiments measured a space charge limited current which was smaller than the modified

Child-Langmuir prediction j_{CL} but larger than the improved bipolar theory j_{IB}. It was hypothesized that this difference could be due ionization of background helium neutrals by the thermoelectrons.[10]

Here, the thermoelectron current from a small (diameter ~ 0.5 mm) hot spot on a tungsten sample exposed to deuterium plasma is measured. These experiments are designed to simulate hot spot formation and arcing from tungsten divertor plates in magnetic fusion devices. The thermocurrent is found to be significantly ($>100\times$) greater than predicted by the improved bipolar theory applied to the unperturbed plasma only. The difference is also attributed to the effect of background neutrals. The importance of background neutrals is confirmed by repeating the experiments in the absence of the background plasma, showing similar levels of thermoelectron current. These experiments indicate that thermoelectron currents from hot spots in plasma-facing components can be significantly larger than unperturbed plasma predictions if significant neutral densities are present.

II. EXPERIMENTAL SETUP

The experiments presented here were performed on the PISCES-B linear plasma device,[11] a steady-state reflex-arc discharge. A schematic of the experimental setup is shown in Fig. 1. Deuterium is used as a fill gas with background neutral pressure $P_N = 5.2$ mTorr. Steady-state plasma conditions in front of the tungsten target sample are measured with a plunging Langmuir probe giving electron density $n_e \approx 10^{13}/\text{cm}^3$, electron temperature $T_e \approx 4$ eV, ion flux $\Gamma_i \approx 8 \times 10^{18}/\text{cm}^2/\text{s}$ (corresponding to ion saturation current $j_{isat} \approx 1\,\text{A}/\text{cm}^2$), and central plasma potential $V_S \approx -8$ V. The neutral density in these plasmas is thus of order $10\times$ higher than the ion density. The floating potential on the tungsten target with plasma on is $V_{float} \approx -23$ V, but the target is typically biased with bias voltage in the range $V_{Bias} = -25$ to -150 V, corresponding to sheath voltages $\phi_{Sheath} = |V_{Bias} - V_S| = 17$ to 142 V.

The tungsten sample target (diameter $D = 25$ mm, thickness $t = 2$ mm) is transiently heated on center with a Nd:YAG laser pulse (wavelength 1064 nm, delivered energy $E \approx 0.5$ J, and pulse length of 1–10 ms), temporarily creating thermoelectron emission from a small (diameter $D \approx 0.5$ mm) hot spot on the tungsten sample surface. The total (net) current emitted from the sample is measured with a Rogowski coil on the target bias cable. Only the transient ($\sim$2 A) current pulse created by the laser hot spot is measured by the Rogowski coil; the steady ($\sim$5 A) background plasma current into the target is measured separately with a shunt resistor. The increased Dα line (H-I 656.1 nm) emission due to the emitted electrons is imaged by a CCD camera and also by a filterscope (interference filter + PMT package, not shown in Fig. 1).

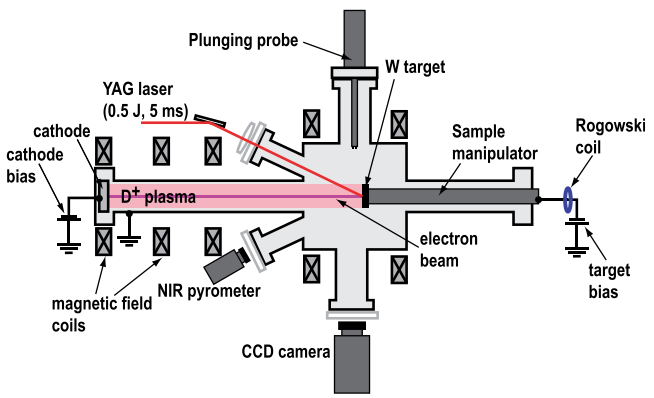

FIG. 1. Schematic of experimental setup.

The electrons leaving the tungsten target are expected to travel axially toward the cathode, due to the axial magnetic field and since the target bias is typically more negative than the cathode bias (-30 V with plasma on or 0 with plasma off). This is supported by CCD images of Dα emission, shown in Fig. 2. Figure 2(a) shows plasma emission, while Fig. 2(b) shows electron beam Dα emission (with background plasma emission subtracted). Figures 2(c) and 2(d) show radial and axial profiles of the beam Dα emission. It can be seen that the thermionic electron beam forms a narrow ($D \approx 5$ mm) filament which attenuates slowly in brightness away from the target, possibly due to energy loss from collisions with background D_2 neutrals.

The fast time evolution of the sample surface temperature during the heating laser pulse is measured with a two color near infra-red (NIR) pyrometer. The pyrometer consists of two separate detectors, one at 1300 nm and one at 1550 nm, each with a bandwidth of 100 nm. The system time response is 10 μs. The individual detectors and other components (image splitter, bandpass filters, fiber optics, etc) are commercially available (e.g., Hamamatsu H10330A-75 PMTs are used), although the system assembly is a custom design. Two pyrometer calibration steps are performed: first, the pyrometer temperature measurement is cross-calibrated with a thermocouple, then the signals are corrected for the small laser spot size using post-mortem analysis of the laser spot size. The thermocouple cross-calibration is obtained during steady-state plasma operation. In this situation, heating is provided by the plasma and cooling can be varied by changing the water flow to the back of the target sample. By varying the cooling flow rate or steady plasma conditions, the steady-state sample temperature can be varied. The small steady-state signal offset due to reflected NIR signal from the hot cathode is corrected by turning off the plasma discharge briefly but leaving the cathode hot. Temperature is obtained from each absolutely calibrated signal (1300 nm and 1550 nm) independently; the two values are then averaged to obtain an average pyrometer reading. A ratio technique is also used as a cross-check to avoid any possible effects of surface emissivity varying with temperature.

In this experiment, where the laser spot size is smaller than the pyrometer spot size, correct interpretation of the pyrometer data requires knowledge of the laser spot size. The above calibration provides sample temperature for a uniform temperature across the entire pyrometer measurement spot size ($D \approx 2$ cm). However, the laser-produced hot spot is much smaller than the laser spot size, so knowledge of the laser spot size is required to interpret the pyrometer data. Due to difficult access in PISCES-B and the small focused laser spot size, direct measurement of the laser spot size at the sample is challenging, so the laser brightness profile on the tungsten target is estimated from post-shot analysis of

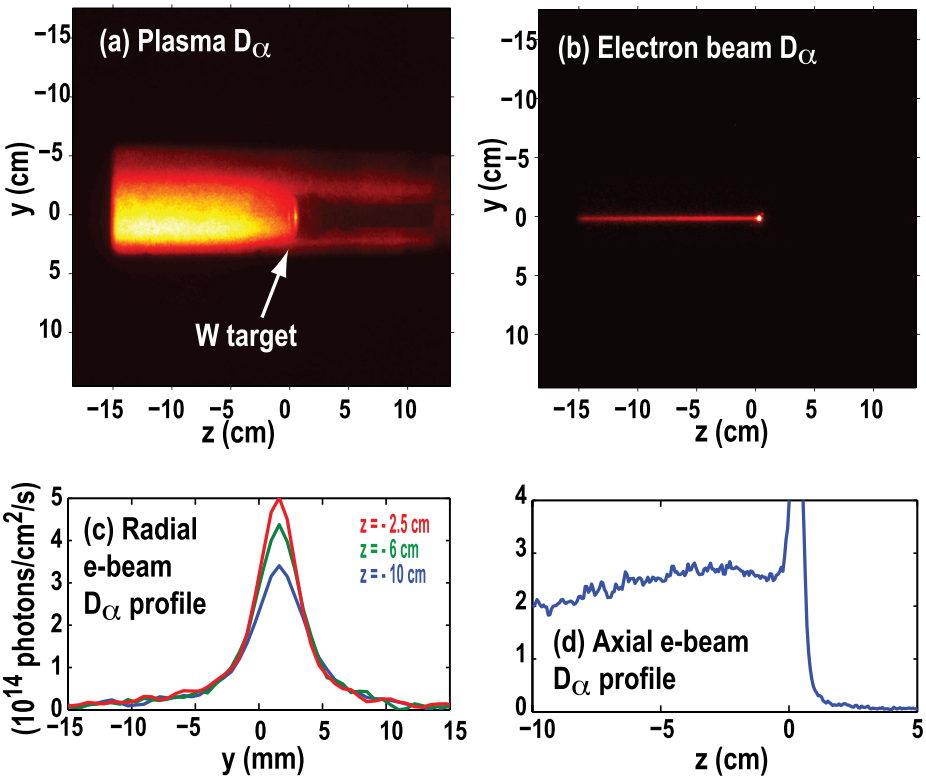

FIG. 2. Dα line emission images of (a) initial target plasma and (b) thermionic electron beam created by laser pulse (with target plasma emission subtracted) as well as (c) radial Dα profile and (d) axial Dα profiles of electron beam.

target samples using a confocal microscope. In front of the focusing lens, the laser brightness profile is found to be well fit by a Gaussian. It is therefore assumed that the laser power deposition on the sample is a Gaussian also. This is expected to be a reasonable approximation, since the *f*-number of the system is large (focal length is 75 cm and lens diameter is 5 cm), so aberrations are expected to be small. The time history of the laser power is known from an external photodiode measurement made during each laser shot. Delivered laser power can then be estimated using the known beamline losses and assuming 50% reflectivity of tungsten.[12] This measured laser power is only a first guess, however, mostly due to uncertainties in the laser window transmission during the experiment and uncertainties in the reflectivity of tungsten. The final deposited power on the sample at a function of time and radius is then assumed to be $P(R,t) = CP_{Meas}(t)\exp(-(R/a)^2)$, where $P_{Meas}(t)$ is the laser power vs time measured with the photodiode, C is a normalization factor, and a is the Gaussian beam radius at the sample. This deposited power is then input into a 2D (cylindrical) heat diffusion solver to calculate surface temperature as a function of radius R and time t. The slight incoming laser angle from the surface normal of $\theta = 15^{\circ}$ is ignored here. The 2D heat diffusion solver includes the temperature dependence of thermal diffusivity of tungsten and radiative cooling of the surface. The deposition depth profile of the laser heat into the tungsten surface is ignored here; this has been shown to be a reasonable approximation for longer (∼ms) laser pulses, although not for shorter (∼ns) laser pulses.[13] Some cooling may be expected due to evaporation of tungsten from the hot material surface. This was estimated using standard vapor pressure curves of tungsten and was found to be negligible in these experiments. Simulated pyrometer signals are then obtained by radially integrating over the radial temperature profile assuming black body radiation and using the steady-state pyrometer intensity calibration.

Tungsten targets heated by laser pulses exhibit a clearly bounded re-crystallization and cracking region, and the radius of this region is used here as a constraint on the laser power scaling factor C and the beam radius at the sample a. The re-crystallization region is found to have a mean grain size which grows pulse-to-pulse and also eventually exhibits cracking. During the laser pulse, the radial profile of laser power causes a temperature gradient, giving compressive stresses on the surface, while cooling of the centrally molten region can cause tensile stresses on the surface.[14,15] A combination of these thermal stresses and brittle-ductile effects then leads to cracking over the re-crystallization region over multiple laser pulses.[16] This is consistent with observations here, where a clear re-crystallization region was observed in a single laser pulse, but then repeated laser pulses were found to sharpen the re-crystallization region due to cracking, but not change the outer diameter of the region. The central melt region, however, was found to grow slowly with number of pulses, possibly due to surface roughening and changing absorption coefficient. For this reason, measured melt diameter is not considered to be a useful constraint. We therefore vary a and C, attempting to best match observed re-crystallization diameter and observed pyrometer signals, in order to determine the beam radius a. Figure 3 shows an example of simulated pyrometer signals and surface melting assuming $a = 0.28$ mm and $C = 1.13$. Fig. 3(a) shows the measured power $P_{Meas}(t)$, as well as the scaled power $CP_{Meas}(t)$. Fig. 3(b) shows measured and simulated pyrometer signals. For plotting purposes, the simulated pyrometer signals are converted to a

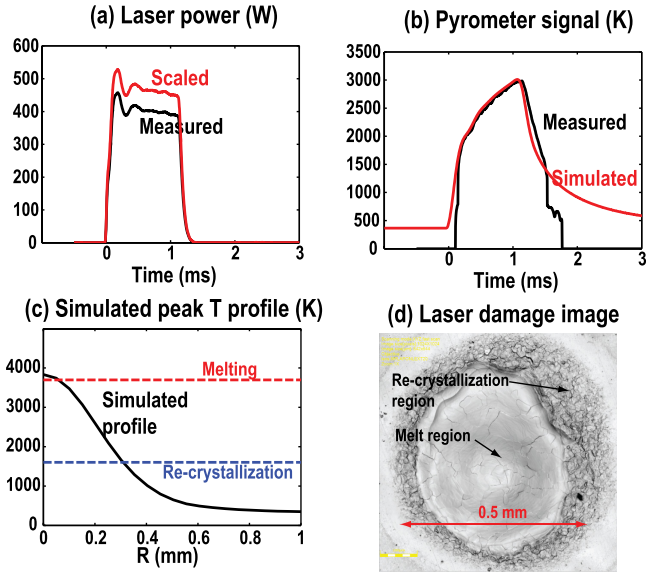

FIG. 3. Simulated pyrometer signals and surface melting assuming beam radius $a = 0.28$ mm and power scale factor $C = 1.13$ showing (a) measured and scaled laser power vs time, (b) measured and simulated pyrometer signals vs time, (c) simulated peak temperature vs radius, and (d) image of laser damage to target showing melt and re-crystallization regions after 100 separate laser shots.

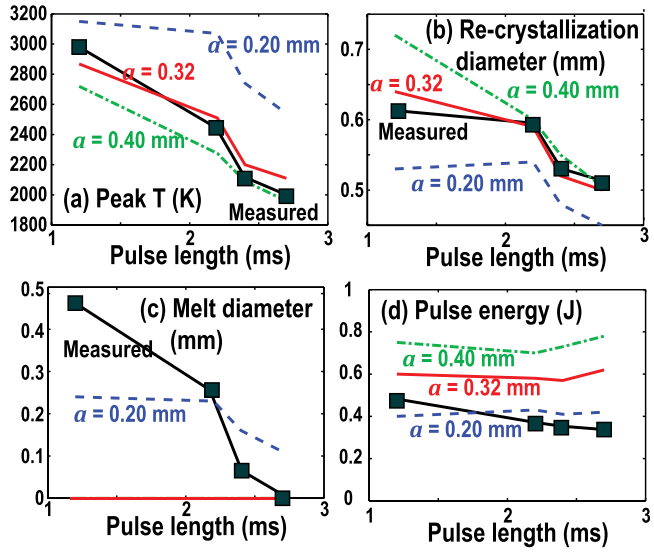

FIG. 4. Fits to four different laser spots, varying dominantly by pulse length, after 100 shots, varying spot diameter $2a$ and pulse energy scale factor C to best match pyrometer temperature and re-crystallization diameter showing (a) measured and fit peak temperature, (b) re-crystallization diameter, (c) melt diameter, and (d) absorbed pulse energy.

temperature assuming a top hat profile with diameter $D = 0.5$ mm, which was also used in the actual pyrometer analysis. Fig. 3(c) shows the simulated peak temperature profile, including melting temperature ($T = 3695$ K) and re-crystallization temperature ($T = 1600$ K). The image shown in Fig. 3(d) and the other images used in this analysis used 100 repeated laser pulses. One source of error in this method is uncertainty in the re-crystallization temperature. Previous experiments found values ranging from 1900 K for pristine tungsten to 1300 K for severely damaged tungsten;[16] an average value of 1600 K is used here. The error in a resulting from this uncertainty in re-crystallization temperature is not large, due to the large temperature gradient at the edge of the laser spot, as seen in Fig. 3(c).

Overall, the fits indicate a beam radius at the target in the range $a \approx 0.3 - 0.34$ mm. This range is roughly consistent with (but more precise than) simple estimates of the laser spot size at the target from geometrical optics using the laser geometry, lens focal length, measured beam profile, and measured beam divergence, giving $a \approx 0.3 - 0.8$ mm. Figure 4 shows examples of fits from four different target laser spots, illustrating the sensitivity of the method to beam radius. The laser pulse length was varied for the four different cases to change the resulting temperature profile on the target, but the optics (and beam radius a) were not varied. Figure 4(a) shows the peak pyrometer temperature, measured and simulated, as well as best fits for three different values of a (trying to match both pyrometer temperature and re-crystallization diameter simultaneously). Figure 4(b) shows the measured (after 100 laser shots) and modeled (assuming a recrystallization temperature of 1600 K) re-crystallization diameter. Figure 4(c) shows the melt diameter and Fig. 4(d) the pulse energy. It can be seen that $a = 0.32$ mm does a reasonably good job of matching pyrometer data and re-crystallization radius in all four cases. The simulations tend to underestimate the melt diameter, probably due to the multi-pulse surface modification effect mentioned above. It can also be seen that the delivered energy, Fig. 4(d), tends to be underestimated slightly, according to this analysis.

Variation of the laser beam radius during the heating pulse is believed to be negligible in these experiments. There is no significant variation of the laser beam profile measured at the laser during the heating pulse. Also, because of the very low plasma density and the long ($\sim$ ms) laser pulse length, which avoids surface ablation, laser-plasma interactions are believed to be negligible here.

III. RESULTS AND ANALYSIS

Using a laser spot size of $a = 0.32$ mm, together with pyrometer time traces and the 2D heat diffusion model, it is possible to quickly reconstruct surface temperatures for different conditions without removing the sample and measuring the re-crystallization diameter. In this faster method of analysis, only the power normalization factor C is scaled as a free parameter to best match the pyrometer data. Figure 5 shows an example of an experiment with the plasma on and target bias $V_{Bias} = -50$ V. Figure 5(a) shows the measured and scaled laser power vs time. Figure 5(b) shows the measured and fit pyrometer signals, as well as the predicted central ($R = 0$) sample temperature vs time. Figure 5(c) shows the net thermoelectron current measured by the Rogowski coil, as well as the gross thermoelectron current calculated from the Richardson-Dushman equation. Also, shown in Fig. 5(c) is the net emission current estimated from the plasma-subtracted electron beam Dα brightness. This is done using the electron-impact cross section for dissociative excitation of D_2 and assuming that all the current is carried by primary thermoelectrons.[17] The electrons were assumed to be

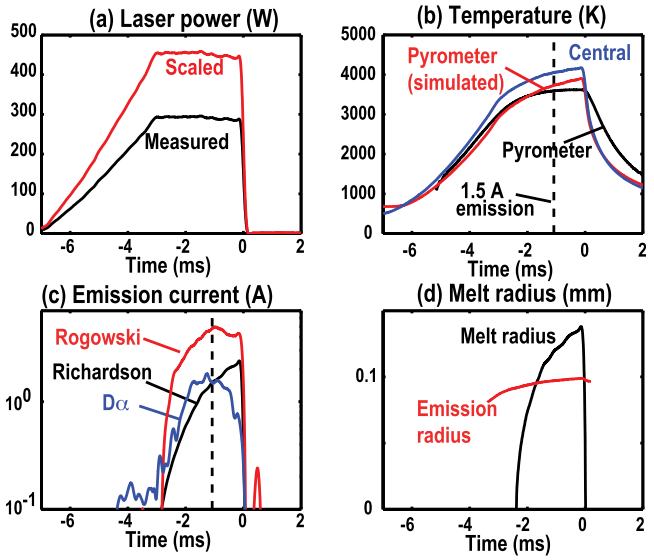

FIG. 5. Laser pulse heating experiment with fits with fixed laser spot size $a = 0.32$ mm showing (a) laser power vs time, (b) pyrometer signal vs time (measured and fit), (c) measured net emission current and predicted gross (Richardson) thermionic emission current, and (d) melt radius vs time.

monoenergetic with energy equal to the sheath potential. Neutral D_2 density is estimated from the measured neutral pressure (5.2 mTorr) using typical (with factor of 2 variation) neutral temperature measured spectroscopically in these plasmas in previous experiments, $T_N = 0.1$ eV.[18] It can be seen that Dα estimate for beam current is roughly consistent (within a factor of 2) with the Rogowski measurement, consistent with the picture that the thermionic electron current is dominantly traveling in a beam from the target back to the plasma cathode. Figure 5(d) shows the predicted melt radius as a function of time. Also plotted is the approximate thermoelectron emission radius at the target; this is needed for analytic estimates of the space-charge limited emission current. Here, we approximate the emission radius r_{emis} from the predicted Richardson thermionic emission current density at the surface: $r_{emis}^2 \approx (2/j_{Rich}(R=0)) \int j_{Rich}(R) R dR$. It can be seen that r_{emis} tends to be smaller than the melt radius, so most of the thermoelectrons in these experiments appear to come from a region of molten tungsten. This is not thought to be important in these experiments though (i.e., surface temperature effects are expected to dominate over surface morphology effects). Also, it can be seen that r_{emis} is much smaller than the Dα emission radius far from the sample of about 3 mm, Fig. 2(c). This is not investigated here, but may result from radial transport due to the strong space charge and resulting strong $E \times B$ rotation in the initially quite narrow electron beam emitted from the surface. Additionally, due to the rather weak axial magnetic field $B = 0.01$ T used in PISCES-B, the electron gyroradius is comparable to the laser spot size, $\rho_e \approx 1$ mm (assuming 10 eV perpendicular energy).

To compare data from experiments with different bias voltages and neutral pressures, and with background plasma on or off, the measured and predicted currents at the point where the gross (Richardson) current equals 1.5 A are chosen, shown by the dashed vertical line in Figs. 5(b) and 5(c).

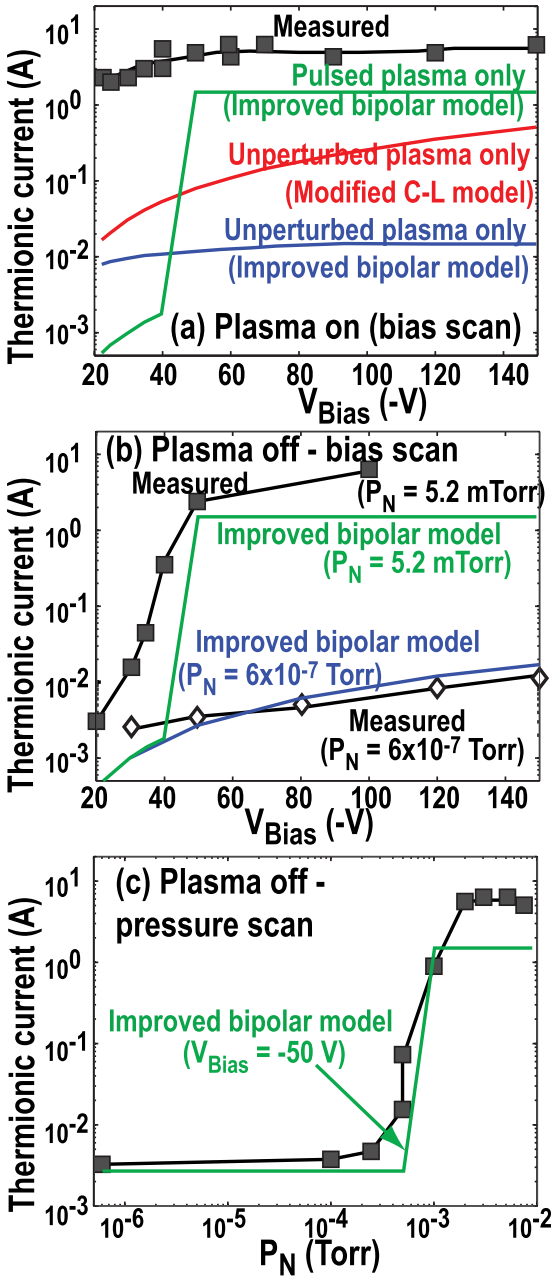

FIG. 6. Measured and predicted net thermionic current taken at a total emission current of 1.5 A showing (a) bias voltage scan with background plasma on and neutral pressure of 5.2 mTorr, (b) bias voltage scan with background plasma off (at high and low pressures), and (c) neutral pressure scan with background plasma off and target bias of −50 V.

This value is chosen because it lies roughly in the center of the emission current pulse, giving good signal levels, as shown in Fig. 5(c).

Figure 6(a) shows the measured (Rogowski) target thermoelectron current as a function of target bias with plasma on and neutral pressure of 5.2 mTorr. It can be seen that the modified Child-Langmuir and improved bipolar predictions applied using the unperturbed plasma only show trends which are similar to the data (rising current with increasing bias voltage) but tend to be of order 100× too small. The improved bipolar prediction, which is expected to be more correct, actually shows worse agreement with the data. We hypothesize that the electron beam creates a small local

plasma through ionization in its current channel, modifying the plasma locally. Although the net emission current from the target is of order 100× smaller than the plasma source current (2 A compared with 170 A), the emission area is 250× smaller ($D = 0.2$ mm for the emission spot compared with $D = 50$ mm for the background plasma) so it is reasonable to expect that the electron beam can strongly perturb the plasma conditions locally within the emission radius.

At present, it is not possible to accurately measure or calculate self-consistently the perturbed plasma parameters in the thermionic electron beam in these experiments. However, it is possible to construct a simple model of the perturbed plasma ion current resulting from ionization of background neutrals. We assume that ions formed by neutral ionization within axial distance $0 < z < L/2$ flow back to the target (ions created in the region $L/2 < z < L$ are assumed to flow into the cathode), where $L = 145$ cm is the cathode-sample distance and we take $z = 0$ to correspond to the target surface. The resulting ion saturation current is then used to determine the allowable space-charge limited electron current released from the target using the improved bipolar model. This situation is unstable: if the neutral ionization source term is sufficiently large, the emission current runs up to its maximum possible value, given either by neutral burn-through or the Richardson current (the latter is expected to be the case in here). Conversely, if the ionization source term is small, the emission current falls down to its minimum value given by unipolar emission. This can be expressed as

$$j_{Neutral} = \begin{cases} j_{Rich}, & \alpha_i > \alpha_{sc} \\ j_{Beam}, & \alpha_i < \alpha_{sc}, \end{cases} \tag{5}$$

where j_{Rich} is given by Eq. (1), and j_{Beam} is the expected unipolar space-charge limited current in the absence of background plasma. For a non-relativistic electron beam with top-hat current profile and radius b, this is roughly[19]

$$j_{Beam} = \frac{I_A}{b^2} \frac{\left(2\tilde{\phi}_w/3\right)^{3/2}}{1/2 + 2\ln(R_w/b)}, \tag{6}$$

where $I_A = 17$ kA, R_w is the grounded wall radius, and $\tilde{\phi}_w \equiv E_{kin}/m_e c^2$ is the normalized electron kinetic energy. Here, we assume the electron kinetic energy to be equal to the sheath potential, $E_{kin} \approx e\phi_{Sheath}$ for the purposes of space-charge flow limitations. In Eq. (5), α_i is the ratio of the system length to ionization mean free path, $\alpha_i \approx \frac{1}{2} L n_{D2} \sigma_i$ and α_{sc} is the space charge limited ratio of ion saturation current to thermoelectron current from the improved bipolar model, Eq. (3). For the ionization cross section σ_i, we use the cross section for direct ionization of D_2, $e + D_2 \rightarrow 2e + D_2^+$, which is expected to be the dominate ionization process here.[20] For the purposes of mean ionization over the long system length, the electron energy is simply assumed to be half the unperturbed sheath potential, $E_{kin} \approx 0.5 e\phi_{Sheath}$. It is likely that there is a perturbation to the plasma space potential in the plasma column by the electron beam, and this will affect the electron kinetic energy in the plasma column and thus the ionization length. This effect was neglected here though for the purposes of calculating the ionization length. The change in plasma space potential resulting from the narrow electron beam cannot be measured by standard methods (Langmuir probe plunges or Doppler shift of spectroscopic lines due to E × B rotation), so is challenging to determine experimentally.

The thermoelectron current predicted by the improved bipolar model, Eq. (5), using only the estimated pulsed plasma ion current, is shown by the green curve in Fig. 6(a). It can be seen that this model is much closer to the measurement for higher bias voltages when compared with the modified Child-Langmuir and improved bipolar models using only the unperturbed plasma. At low bias voltages, the perturbed plasma model fails badly, possibly due to the neglect of the background plasma in the simplified model. This is consistent with data taken with the plasma turned off, shown in Fig. 6(b). At the same background neutral pressure, the higher bias voltage data are similar to the "plasma-on" data, Fig. 6(a). However, at lower bias voltages, the "plasma-off" data are much lower, consistent with the background plasma dominating the thermoelectron current at low bias voltages. A bias voltage scan was done with no plasma and no background neutrals, shown in Fig. 6(b) as hollow diamonds. In this case, the measured current is extremely low, in agreement with the pulsed plasma model. Finally, a neutral pressure scan was performed at fixed bias voltage and with no plasma. As predicted by the pulsed plasma neutral ionization model, a sudden transition from low thermoelectron current to high thermoelectron current is observed, Fig. 6(c). This sudden transition supports the basic physics of the pulsed plasma model, i.e., that the observed thermoelectron current pulse arises dominantly from a pulsed plasma created temporarily by background neutral ionization. Field emission has been ignored here and is thought to be small because of the huge increase in electron current seen as temperature is increased, Fig. 5(c), consistent with thermionic emission. Also, because of the continuous sample surface melting and re-crystallization, the tungsten surface is expected to be relatively smooth, and thus not susceptible to large field emission.

IV. SUMMARY

Overall, this work demonstrates that simply using the initial background plasma for estimating space-charge limited thermoelectron current from a hot spot on a plasma-facing surface can be incorrect in the presence of significant neutral density. The emitted electrons can ionize the background neutrals, which can significantly increase the allowable thermoelectron current. A rapid bifurcation can occur with increasing neutral pressure, where the thermoelectron current suddenly jumps to a maximum set by either the Richardson level (the case in these experiments) or by neutral burn-through (possibly the case in situations with a broader emission radius). These results are expected to be relevant to many magnetic fusion energy experiments, where plasma-facing surface layers quickly (usually within several seconds or less) become saturated with hydrogen and neutral flux out of the walls is comparable to plasma flux into the wall. In these cases, neutral densities near the wall are

expected to be comparable or greater than the plasma density, so space charge limited thermoelectron current from hot spots could be greater than estimated from the background plasma ion saturation current alone, thus resulting in a modification of surface erosion rates due to arcing. The present work does not derive a careful expression for thermoelectron current in the presence of both background plasma and neutrals. As can be seen in Fig. 6(a), the present simple neutral ionization model ignoring background plasma fails badly at low bias voltages. Future work will therefore need to develop a self-consistent model for space-charge limited thermoelectron current, including both neutrals and background plasma.

ACKNOWLEDGMENTS

Helpful discussions with Professor S. Krasheninnikov are gratefully acknowledged. This work was supported by U.S. DOE Grant No. DE-FG02-07ER54912.

[1]G. M. McCracken and P. E. Scott, Nucl. Fusion **19**, 889 (1979).
[2]S. Kajita, N. Ohno, Y. Hirahata, and M. Hiramatsu, Fusion Eng. Des. **88**, 2842 (2013).
[3]A. V. Nedospasov and I. V. Bezlyudny, Contrib. Plasma Phys. **38**, 337 (1998).
[4]V. Philipps, U. Samm, M. Z. Tokar, B. Unterberg, A. Pospieszczyk, and B. Schweer, Nucl. Fusion **33**, 953 (1993).
[5]A. C. Marshall, Appl. Phys. Lett. **73**, 2971 (1998).
[6]G. D. Hobbs and J. A. Wesson, Plasma Phys. **9**, 85 (1967).
[7]N. Ohno, E. Shimizu, and S. Takamura, Contrib. Plasma Phys. **36**, 386 (1996).
[8]T. Kuwabara, N. Ohno, S. Takamura, and M. Y. Ye, J. Plasma Fusion Res. **77**, 464 (2001), see http://ci.nii.ac.jp/naid/110003827615/en.
[9]S. Takamura, N. Ohno, M. Y. Ye, and T. Kuwabara, Contrib. Plasma Phys. **44**, 126 (2004).
[10]Y. Hagino, N. Ohno, S. Takamura, and M. Y. Ye, J. Nucl. Mater. **313**, 675 (2003).
[11]R. P. Doerner, M. J. Baldwin, and K. Schmid, Phys. Scr., **T111**, 75 (2004).
[12]J. H. Yu, R. P. Doerner, T. Dittmar, T. Hoschen, T. Schwarz-Selinger, and M. J. Baldwin, Phys. Scr., **T159**, 014036 (2014).
[13]J. H. Bechtel, J. Appl. Phys. **46**, 1585 (1975).
[14]N. Farid, S. S. Harilal, O. El-Atwani, H. Ding, and A. Hassanein, Nucl. Fusion **54**, 012002 (2014).
[15]S. E. Pestchanyi and J. Linke, Fusion Eng. Des. **82**, 1657 (2007).
[16]A. Suslova, O. El-Atwani, D. Sagapuram, S. S. Harilal, and A. Hassanein, Sci. Rep. **4**, 6845 (2014).
[17]K. Sawada, K. Eriguchi, and T. Fujimoto, J. Appl. Phys. **73**, 8122 (1993).
[18]E. M. Hollmann, A. Yu. Pigarov, and Z. Yan, Phys. Plasmas **13**, 052510 (2006).
[19]T. C. Genoni and W. A. Proctor, J. Plasma Phys **23**, 129 (1980).
[20]D. Reiter, *The Data File AMJUEL: Additional Atomic and Molecular Data for EIRENE* (Forschungszentrum Juelich GmbH, 2004).